plasma

Article

Microanalysis of Active Nitrogen Oxides (RONS) Generation Characteristics during DC Negative Corona Discharge at a Needle-Plate Electrode

Jinqiang Shi, Fubao Jin *, Shangang Ma, Xinhe Liu, Xuejian Leng and Keyuan Chen

School of Energy and Electrical Engineering, Qinghai University, Xining 810016, China; shijinqiang1011@163.com (J.S.); msgqhu@139.com (S.M.); 17320146085@163.com (X.L.); 19818274545@163.com (X.L.); 15129147646@163.com (K.C.)
* Correspondence: jinfubao@163.com

Abstract: The DC negative corona of needle-plate electrodes can generate atmospheric pressure low-temperature plasma active particles, which have important effects on biological mutagenesis. The DC negative corona discharge of an air needle-plate electrode with effective consideration of NO_x particles was simulated and the Trichel pulse current was obtained, focusing on the development of particles and the distribution of active nitrogen oxides (RONS) at four moments in the pulse process. The simulation results indicate that the positive ions ($N_2{}^+$ and $O_2{}^+$) and negative ions (O^- and $O_2{}^-$) were closely related to the current changes, and the negative ions (O^- and $O_2{}^-$) presented a typical stratification phenomenon. RONS (H_2O_2, O_3, and NO) were approximately uniformly distributed above the level of the plate electrode at the same instant, with H_2O_2 and O_3 except for the area below the needle tip. They trended to a cumulative increase in concentration with time. This study provides a theoretical basis for corona discharge plasma seed treatment technology.

Keywords: negative corona; nitrogen oxides; microscopic; Trichel pulse

check for updates

Citation: Shi, J.; Jin, F.; Ma, S.; Liu, X.; Leng, X.; Chen, K. Microanalysis of Active Nitrogen Oxides (RONS) Generation Characteristics during DC Negative Corona Discharge at a Needle-Plate Electrode. *Plasma* **2023**, *6*, 649–662. https://doi.org/10.3390/plasma6040045

Academic Editor: Andrey Starikovskiy

Received: 14 August 2023
Revised: 14 October 2023
Accepted: 19 October 2023
Published: 27 October 2023

1. Introduction

Corona discharge is a partial self-sustained discharge phenomenon held by an extremely inhomogeneous electric field, which usually occurs in the vicinity of the tip electrode. Compared to other forms of discharge, corona discharge devices are characterized by their simple structure, low cost, and ability to be utilized on a large scale [1]. It is owing to these promising properties that corona discharge has been widely applied in the fields of electrostatic dust removal [2,3], pollutant treatment [4], surface treatment [5], and bio-mutagenesis [6]. In addition, the high-voltage corona electrical field seed treatment technology is a new physical mutagenesis technology, characterized by a simple device, obvious biological effects, and environmental friendliness [7]. It has been revealed that a large number of plasma active particles active oxygen (ROS), active nitrogen (RNS) as well as electric-field distribution are generated during the discharge process, and these physicochemical elements act complexly on the seed thereby activating the seed vitality [8].

The corona characteristics of different polarities differ greatly and can be divided into negative and positive corona according to polarity. Liu M et al. conducted DC corona discharge experiments on a needle-plate corona discharge model under different DC voltage conditions. The results showed that the positive corona gradually went through several different discharge stages, including initial streaming discharge, periodic streaming discharge, glow discharge, and spark discharge, as the voltage was increased. The negative corona gradually went through the early and middle stages of Trichel discharge, sawtooth discharge, and glow discharge. Compared to the positive corona, the negative corona has a smaller pulse amplitude and time interval, but it has a better uniformity and higher repetition rate [9].

E. Moreau et al. studied the positive and negative corona discharge of needle-plate structure in air and found that the positive corona discharge produced a faster ion wind speed but the effective radius was relatively small [10]; the ion distribution of the negative corona discharge obviously has a larger range [11], and it is obvious that the negative corona electric field can be more widely and stably applied to plant seed mutagenesis. However, the negative corona current is composed of a series of regular pulsed currents known as Trichel pulses [12]. Numerical simulation, as an effective tool complementing experiments, can provide valuable insights into the experiments and even play a decisive role in the overall study. In the study of gas discharge mechanisms, numerical simulation has become an effective tool due to the limitation of experimental methods in space plasma. In the literature [11,13], the DC negative corona of needle-plate electrodes in air was simulated, and the development of the Trichel pulse of the negative corona was explained in detail; however, the hydrodynamic simulation model used in the simulation could only macroscopically analyze the distribution characteristics of positive ions, negative ions, and electrons. In the literature [14], a hybrid numerical model was used to analyze the physical development of air discharges at low pressure, and 27 plasma chemical reactions that best reflect the microphysical processes of particles in air discharges were summarized. In the literature [15], the negative corona discharge model for rod-plate electrodes was improved on the basis of the hydrodynamic model by combining the collision reaction model, and the temporal and spatial development of the electric-field strength, the plasma chemical reaction rate, the space charge density, and the electron density distribution in the Trichel pulse process were analyzed.

In the literature [16,17], a hybrid numerical model was improved for the hydrodynamic model, and a large number of plasma chemical reactions were included in the model to explain the development of the Trichel pulse in terms of specific particle distributions. However, the composition of air is complex, and the discharge process is inevitably accompanied by the generation of activated nitrogen oxides (RONS), so it is necessary to consider a more comprehensive plasma chemical reaction system and analyze the biological pattern of RONS as a refinement of the negative corona–Trichel pulse mechanism in the simulation process.

Plasma can promote seed awakening and seed germination and growth, and kill fungal bacteria on the seed-coat surface [18]. Wang Min et al. studied the effects of different voltage intensity atmospheric pressure plasma treatments on lettuce seed development and yield situation. The results showed that the effects of different degrees of voltage and atmospheric pressure varied significantly. Among them, the appropriate voltage treatment obviously promoted the seed vigor and germination, but the treatment with too high a dose did not promote, as well as even inhibit, the germination of seeds [19]. Reaction oxygen species (ROS) are by-products of aerobic metabolism in plants. ROS are continuously produced in plants, and when their levels exceed the threshold, they cause damage to plant-cell membranes. Therefore, the enzymatic scavenging system formed in the plant cell regulates it in a state of dynamic equilibrium. Hydrogen peroxide (H_2O_2) accumulated during seed suckering is essential for breaking seed dormancy [20]. Nitric oxide (NO) is the most abundant reactive nitrogen in plants, and since plants cannot synthesize it themselves, they can only accumulate and metabolize atmospheric NO [21]. In its interaction with plant hormones, NO has different accumulation levels for different cells, so the role of NO in plant-hormone responses remains a complex issue. In conclusion, small molecules have a regulatory role in seed germination.

ROS and RNS have a wide range of regulatory functions in various plant growth and development processes, including plant germination, physiological and biochemical metabolism, and signaling [22]. Exogenous hydrogen peroxide (H_2O_2), ozone (O_3), and nitric oxide (NO) as typical ROS and RNS are able to promote seed germination and growth as well as resistance properties [23]. Sodium nitroprusside (SNP) as a form of exogenous NO can break seed dormancy, as in Arabidopsis and barley [24]. The dormancy of seeds can also be broken, and germination promoted using exogenous ROS [25,26]. DC negative corona under needle-plate electrodes, as one of the common ways of plasma generation, produces a variety of RONS in air discharges that can affect the growth of plants [27,28]. Plasma-activated water (PAW) produced by gas–liquid discharges is rich in active nitrogen oxides (NO_2^-, NO_3^-, O_3, as well as H_2O_2), and studies have demonstrated that PAW could promote the germination growth of plant seeds in close correlation with RONS [29,30]. However, the active nitrogen oxides in PAW inevitably derive from gas discharges. Therefore, it is valuable to carry out the microscopic generation as well as the distribution pattern of RONS in DC negative corona air discharges of needle-plate electrodes.

In this paper, a two-dimensional hydrodynamic and chemical model of the DC negative corona of needle-plate electrode with complex air at atmospheric pressure is established, which has 14 species and 34 kinds of chemical reactions, and the validity of the plasma chemical reaction system is verified by simulation and the Trichel pulse current of negative corona discharge is obtained. The development of particles at four moments during the pulse and the distribution of RONS above the lower plate are emphasized. In this study, the needle-plate electrode DC negative corona discharge in air with effective consideration of NO_x particles was simulated, while providing a theoretical basis for corona discharge plasma seed treatment technology.

2. Numerical Modeling

2.1. Discharge Structure and Boundary Conditions

As shown in Figure 1, a two-dimensional plasma hydrodynamic and chemical model of needle-plate electrode for atmospheric pressure air is investigated in this paper. Since the needle-plate model has symmetry, two-dimensional axisymmetric modeling was used for the analysis. The radius of curvature of the needle was 0.12 mm, the lower pole plate was grounded, the gap distance was 3 mm, and the applied voltage was −2 kV. In the model, the setup of the boundary conditions was of great importance, where the electrons will be lost in the walls as well as surface reactions due to the secondary electron emission effect.

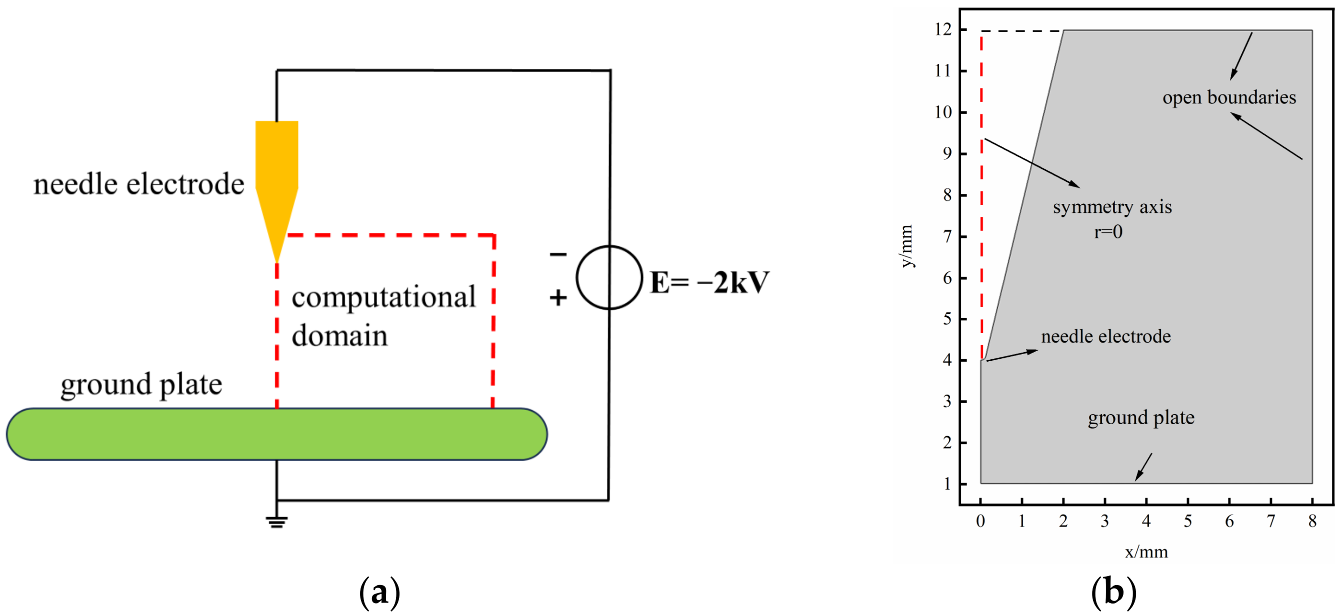

Figure 1. Needle-plate negative corona discharge model: (**a**) Needle-plate electrode structures; (**b**) The computational domain for the 2D axisymmetric model.

The electron fluxes are set at the cathode as well as the anode boundary conditions:

$$\mathbf{n} \cdot \boldsymbol{\Gamma}_e = \frac{1}{2} v_{e,th} n_e - \sum_p \gamma_p (\boldsymbol{\Gamma}_p \cdot \mathbf{n}) \tag{1}$$

Heavy matter ions were lost on the wall by surface reactions and the electric field wass directed toward the wall:

$$\mathbf{n} \cdot \mathbf{j_k} = M_k R_k + M_k c_k Z_k \mu_k (\mathbf{E} \cdot \mathbf{n}) [Z_k \mu_k (\mathbf{E} \cdot \mathbf{n}) > 0] \tag{2}$$

where $\boldsymbol{\Gamma}_e$, $v_{e,th}$, γ_p, n_e and $\mathbf{n}$ are the electron flux vector, the electron thermal velocity, the secondary electron emission coefficient, the electron density, and the outward normal, respectively; M_k, R_k, c_k, Z_k, μ_k and $\mathbf{E}$ denotes the molar mass of species k, the surface reaction rate of species k, the mass fraction of heavy species k, the charge number for species k, the mobility of species k, and the electric field, respectively. The p subscript means the p-type positive ion in the reaction system in the sum.

2.2. Control Equations

The model was calculated by solving the coupled electron transport equation, the heavy matter transport equation, and the Poisson equation, represented as follows:

The electron continuum equation is:

$$\frac{\partial}{\partial \mathrm{t}}(n_e) + \nabla \cdot [-(\mu_e \cdot E) n_e - D_e \cdot \nabla n_e] = R_e \tag{3}$$

The heavy substance transport equation is:

$$\rho \frac{\partial}{\partial \mathrm{t}}(\varpi_k) + \rho(\mathbf{u} \cdot \nabla) \varpi_k = \nabla \cdot \mathbf{j_k} + R_k \tag{4}$$

$$R_k = \int_0^\infty \varepsilon^{1/2} f(\varepsilon) \sigma(\varepsilon) d(\varepsilon) \tag{5}$$

$$D_e = \mu_e T_e \tag{6}$$

where $\mathbf{u}$, μ_e, D_e and T_e are the electron mobility, the electron diffusion coefficient, and the electron temperature, respectively; R_e is the electron source term; ρ, ϖ_k, j_k, $\mathbf{u}$ and R_k denote the mixture density, the mass fraction of heavy particles k, the diffusion flux vector, the mean fluid velocity vector, and the rate expression for species k, respectively. $f(\varepsilon)$ is the electron energy distribution function and ε is the average electron energy [31]. $\sigma(\varepsilon)$ is the collision intercept of the reaction [32].

The Poisson equation is:

$$\nabla \cdot \varepsilon_0 \varepsilon_\mathrm{r} E = \rho \tag{7}$$

$$E = -\nabla V \tag{8}$$

where V is the space potential, ε_0 and ε_r are the vacuum permittivity and relative permittivity, respectively, and ρ is the space charge density.

2.3. Type of Crash Response

The discharge model in this paper used a simplified air–chemical reaction system, which was N_2:O_2 = 4:1, including 34 chemical reactions and 14 species: e, N_2, O_2, $N_2{}^+$, $O_2{}^+$, $O_2{}^-$, O, O^-, N, O_3, NO, NO_2, N_2O, and NO_3. The chemical reactions of the plasma are shown in Table 1 [33,34].

Table 1. Major particle chemical reactions.

Number	Reaction	Rate Coefficient
R1	$e + N_2 => e + N_2$	$f(\varepsilon)$
R2	$e + N_2 => N_2^+ + 2e$	$f(\varepsilon)$
R3	$e + O_2 => e + O_2$	$f(\varepsilon)$
R4	$e + O_2 => O_2^-$	$f(\varepsilon)$
R5	$e + O_2 => O + O^-$	$f(\varepsilon)$
R6	$e + O_2 => O_2^+ + 2e$	$f(\varepsilon)$
R7	$e + 2O_2 => O_2 + O_2^-$	$5.17 \times 10^{-43} T_e{}^{-1}$
R8	$e + N_2 + N_2^+ => 2N_2$	$6.07 \times 10^{-34} T_e{}^{-2.5}$
R9	$2e + N_2^+ => N_2 + e$	$7.18 \times 10^{-39} T_e{}^{-4.5}$
R10	$O_2^+ + e => 2O$	$6.25 \times 10^{-15} T_e{}^{-1}$
R11	$N_2^+ + e => 2N$	$2.8 \times 10^{-13}(300/T_e)^{0.5}$
R12	$e + O_3 => O_2 + O^-$	1×10^{-17}
R13	$e + O_2^+ => O_2$	4×10^{-18}
R14	$2e + O_2^+ => O_2 + e$	$7.18 \times 10^{-39} T_e{}^{-4.5}$
R15	$e + N_2^+ => N_2$	$7.72 \times 10^{-14} T_e{}^{-0.5}$
R16	$O_2^- + O_2^+ => 2O_2$	2×10^{-13}
R17	$O_2 + N_2^+ => N_2 + O_2^+$	$1.04 \times 10^{-15} T_g{}^{-0.5}$
R18	$O_2^+ + O_2 + O_2^- => 2O_2 + O_2$	2×10^{-37}
R19	$O_2^+ + N_2 + O_2^- => 2O_2 + N_2$	2×10^{-37}
R20	$O + O_2 + N_2 => O_3 + N_2$	2.5×10^{-46}
R21	$O + O_2 + O_2 => O_3 + O_2$	2.5×10^{-46}
R22	$O^- + O_2^+ => O + O_2$	$3.46 \times 10^{-12} T_g{}^{-0.5}$
R23	$O_3 + N => NO + O_2$	6×10^{-19}
R24	$O + NO_2 => NO + O_2$	$2.63 \times 10^{-17} exp(-13{,}790/T_g)$
R25	$O_2 + N => NO + O$	$1.0 \times 10^{-31}(300/T_g)^{2.5}$
R26	$O_3 + NO_2 => NO + 2O_2$	$1.0 \times 10^{-31}(300/T_g)^{2.5}$
R27	$O_3 + NO => NO_2 + O_2$	$3.6 \times 10^{-18} exp(-1560/T_g)$
R28	$O + N_2O => 2NO$	$1.66 \times 10^{-16} exp(-14{,}090/(T_e)$
R29	$3NO => NO_2 + N_2O$	$2.95 \times 10^{-50} exp(-13{,}490/T_e)$
R30	$NO + N_2O => NO_2 + N_2$	$4.17 \times 10^{-16} exp(-25{,}160/T_e)$
R31	$2NO_2 => NO_3 + NO$	$5.37 \times 10^{-18} exp(-12{,}880/T_e)$
R32	$NO + NO_3 => 2NO_2$	$1.6 \times 10^{-17} exp(150/T_g)$
R33	$O_3 + NO_2 => NO_3 + O_2$	$1.2 \times 10^{-19} exp(-2450/T_g)$
R34	$NO + NO_3 => 2NO + O_2$	$2.71 \times 10^{-17} T_g{}^{-0.23} exp(-947/T_g)$

Note: The reaction rate constants in Table 1 are in m^3/s for two-body collisions, m^6/s for three-body collisions, and K for T_g and T_e.

3. Results and Discussion

This paper was based on the plasma module of COMSOL Multiphysics for modeling and analysis, with an ambient pressure of 1 atm, a temperature of 300 K, and a total of 273,021 cells in the computational grid, to study the process of Trichel pulsed-current discharge and the generation and distribution pattern of RONS.

3.1. Validation of the Validity of Chemical Reaction Systems

To ensure that the chemical reaction system had the property of predicting the generation pattern of the reaction products, this paper imported the chemical reaction system into the Dielectric Barrier Discharge (DBD) model under the same experimental conditions (V_{am} = 0.6 kV, f = 15 kHz, air gas gap pressure of 500 Pa). Comparing the experimental and simulated voltage and current waveforms, as shown in Figure 2, the current waveform morphology was similar between the two, and the discharge breakdown phase was basically the same [35]. Therefore, the chemical system used in this model was capable of qualitatively analyzing the DC negative corona discharge products of the needle-plate electrode.

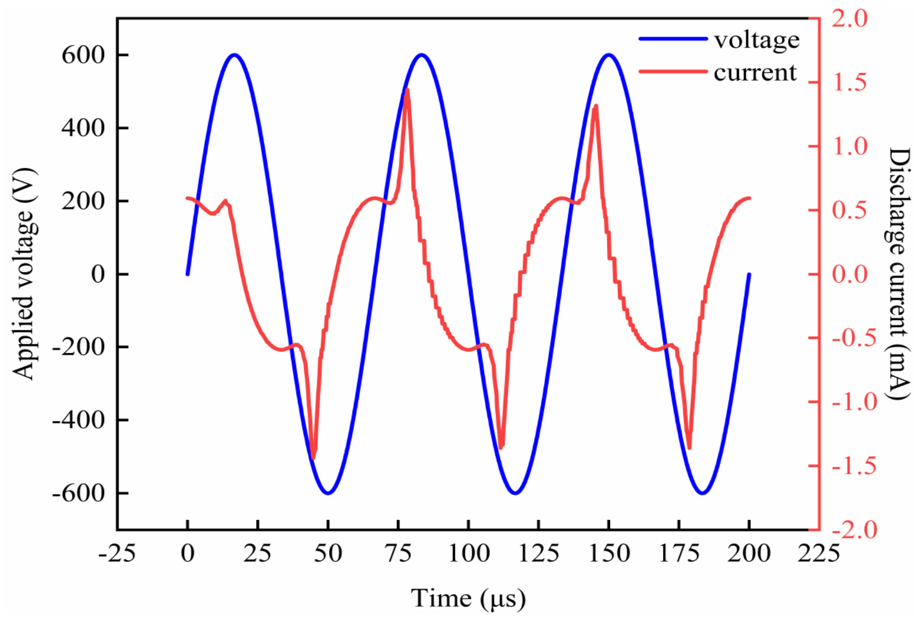

Figure 2. Voltage and current waveform verification of the reaction system [35].

3.2. Discharge Current of Negative Corona

Figure 3 shows the current waveform of the Trichel pulse with a negative corona under the needle-plate gap, the pulse has the characteristics of rapid rise and slow fall, and as shown in Figure 4, a multilayered distribution of negative ions appeared with the Trichel pulse, the Trichel pulse appears to have a multilayered negative ion distribution, which indicates that the simulation results have credibility [11]. In this paper, the microphysical changes of particles were specifically analyzed with four moments of the 6th pulse (t_1: 2.05 μs, t_2: 2.10 μs, t_3: 2.20 μs, t_4: 2.30 μs). The blue symbols represent the four selected moment points, and the red lines represent the current pulse variations, while the dashed lines represent the local plots within this range.

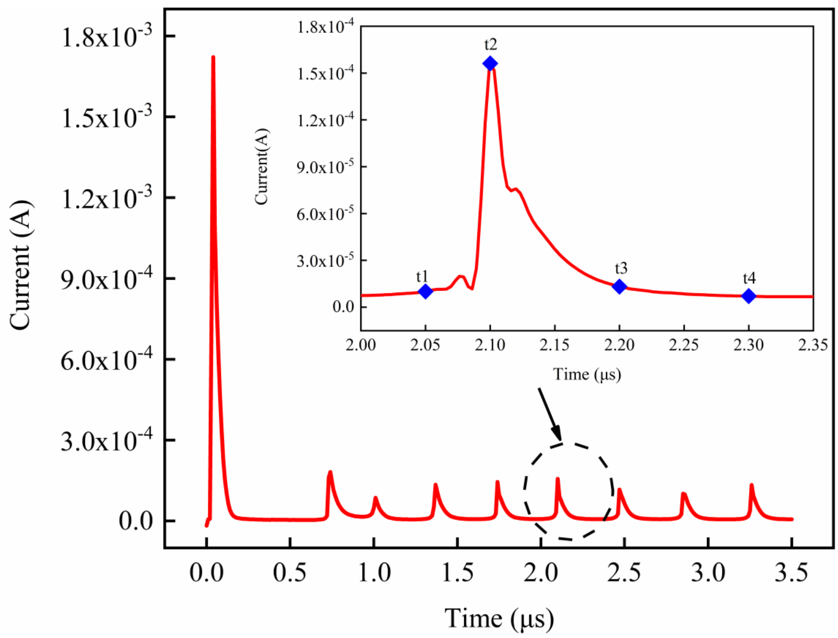

Figure 3. Corona current waveform.

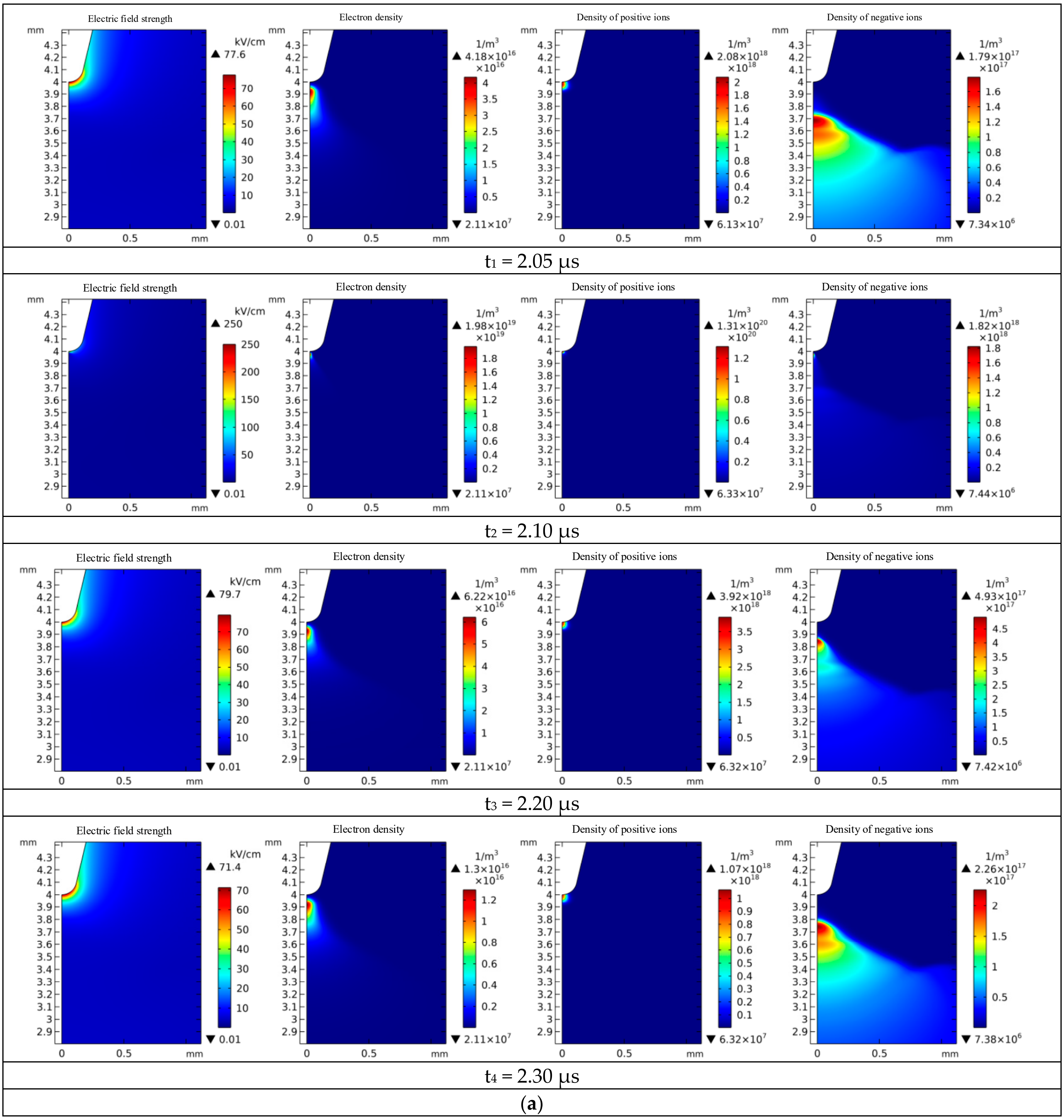

Figure 4. *Cont.*

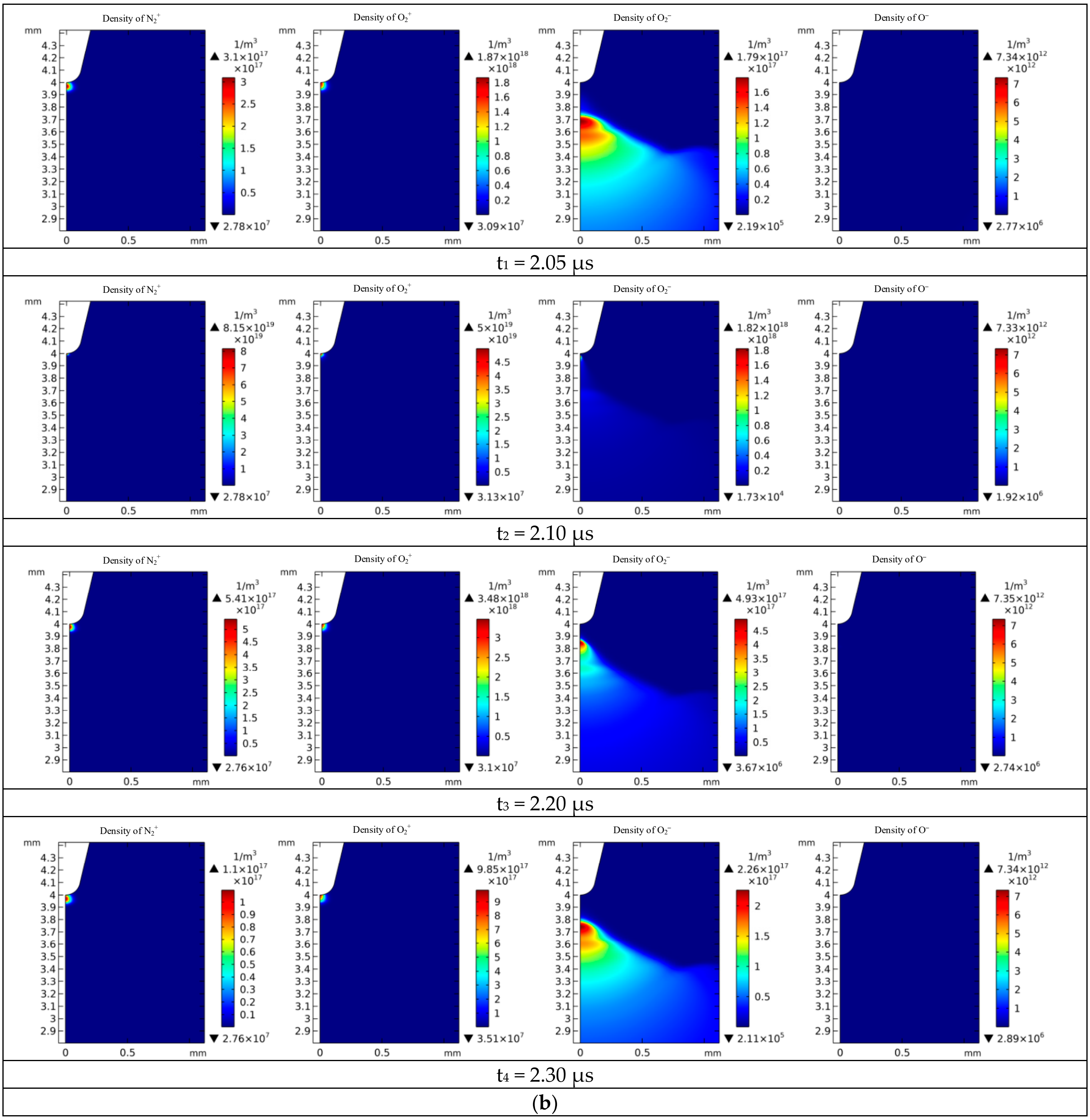

Figure 4. The ion distribution during the Trichel pulse: (**a**) The electric field strength, the electron density, the density of positive ions, and the density of negative ions at 4 moments; (**b**) The number density of N_2^+, O_2^+, O_2^-, and O^- at 4 moments.

3.3. Ionic Behavior during Discharge

The major positive ions considered in the model were N_2^+ and O_2^+, and the negative ions were both O^- and O_2^-. As shown in Figure 4a, the positive ions in space at the moment t_1 were at the end of the previous pulse as well as at the beginning of the next pulse, and were present only near the cathode, where the number densities of N_2^+ and O_2^+ reached 2.08×10^{18} m^{-3}. With the rapid rise of current, the number density of positive ions grew significantly and compressed toward the cathode surface. The cathodic-sheath layer was fully formed, and by the moment t_2 of the peak current, the number density of positive ions reached 1.31×10^{20} m^{-3}. At moments t_3 to t_4, the number densities of N_2^+ and O_2^+ continued to decrease, but the positive ion density at the cathode remained at 1.07×10^{18} m^{-3}. This indicates that the rising and falling processes of the Trichel pulse corresponded to the development of rising and falling cathodic-sheath positive ions.

As shown in Figure 4a, at the moment t_1, the field strength near the needle tip reached 77.6 kV/cm, which was much larger than the air breakdown electric-field strength of 30 kV/cm, thus making the air ionize rapidly. Positive ions produced secondary electrons on the cathode surface to form an electron collapse, and the electrons formed negative ions O^- and O_2^- due to the oxygen-attachment reaction, with a number density of 1.79×10^{17} m^{-3}. As the current pulse rose to the peak moment t_2, the electric-field strength continued to increase by 250 kV/cm, and the particles near the needle tip reacted violently, the electron density increased significantly, and the corresponding negative ion density also increased. The negative ions and electrons moved away from the cathode under the force of the electric field, and the number densities of the positive ions, negative ions, and electrons reached a maximum of 1.31×10^{20} m^{-3}, 1.82×10^{18} m^{-3}, and 1.98×10^{19} m^{-3}, respectively. At the moments from t_2 to t_4, electrons and negative ions continued diffusing to the anode, the number density of the electrons decreased, and the adsorption capacity decreased due to the migration of the electric field to the anode as well as the weakening, while the number density of the negative ions decreased continuously. As the negative ions continued to strengthen away from the cathode, the electric field strength near the needle tip was re-centralized (it can be considered that the electric field strength recovered from 71.4 kV/cm to 77.6 kV/cm from the moment t_4 to the moment t_1 of the next pulse), a process that ensured the continuity of the pulse.

As shown in Figure 4b, by analyzing and comparing the maximum number densities of N_2^+ ions, it can be seen that the maximum number densities of N_2^+ ions were 3.1×10^{17} m^{-3}, 8.15×10^{19} m^{-3}, 5.41×10^{17} m^{-3}, and 1.1×10^{17} m^{-3} at moments t_1 to t_4, respectively. With time, the number density of N_2^+ ions reached a maximum at the peak current moment t_2 then gradually decreased from t_3 to t_4. By a similar analysis, the maximum number densities of the O_2^+ ions were 1.87×10^{18} m^{-3}, 5.0×10^{19} m^{-3}, 3.48×10^{18} m^{-3}, and 9.85×10^{17} m^{-3} at moments t_1 to t_4, respectively. With time, the number density of the O_2^+ ions reached a maximum at the peak current moment t_2 then gradually decreased from t_3 to t_4. By analyzing the pattern of change of the two positive ions, it can be concluded that the rising and falling processes of the Trichel pulse still corresponded to the development of cathodic-sheath positive ions. The maximum number densities of the O_2^+ ions were higher than the maximum number densities of the N_2^+ ions by nearly an order of magnitude at moments t_1, t_3, and t_4. At moments t_1 to t_4, the minimum number density of the O_2^+ ions (3.09×10^7 m^{-3}, 3.13×10^7 m^{-3}, 3.1×10^7 m^{-3}, and 3.51×10^7 m^{-3}) was similarly higher than the minimum number density of N_2^+ ions (2.78×10^7 m^{-3}, 2.78×10^7 m^{-3}, 2.76×10^7 m^{-3}, and 2.76×10^7 m^{-3}), respectively. Although the maximum number densities of the O_2^+ ions and N_2^+ ions were in the same order of magnitude at moment t_2, the overall analysis shows that O_2^+ ions were the more numerous positive ions.

By analyzing and comparing the maximum number densities of the O_2^- ions, it can be seen that the maximum number densities of O_2^- ions were 1.79×10^{17} m^{-3}, 1.82×10^{18} m^{-3}, 4.93×10^{17} m^{-3}, and 2.26×10^{17} m^{-3} at moments t_1 to t_4, respectively. With time, the number density of the O_2^- ions reached a maximum at the peak current moment t_2 then gradually decreased from t_3 to t_4. However, the maximum number density of the O^- ions remained almost unchanged. At each moment, the maximum number density of O_2^- ions was much higher than that of the O^- ions, while the cloud-graph distribution of O_2^- ions was more obvious. Therefore, O_2^- ions were the main negative ions.

3.4. Generation Pattern of ROS

3.4.1. Generation Pattern of Ozone (O_3)

Ozone (O_3) has strong oxidizing properties, and the use of ozone to treat seeds before planting crops can improve seed germination and kill pathogenic microorganisms [26]. The production of ozone in air discharge is mainly provided by three-body collision reactions ($O + O_2 + O_2 => O_3 + O_2$, $O + O_2 + N_2 => O_3 + N_2$), while the production of O plays a major effect on the production of ozone in air, and O is mainly provided by the reactions ($e + O_2 => O + O^-$, $e + O_2^+ => 2O$, $O^- + O_2^+ => O + O_2$, $O_2 + N => NO + O$). The leftmost side of the complete needle-plate electrode boundary was used as the 0 start point, and since most of the biological objects treated based on the needle-plate structure were placed above the plate electrode, the distribution of particles was viewed in this paper at a level of 1 mm from the grounded electrode plate. As shown in Figure 5, the density of the O on the 1 mm surface of the plate electrode from t_1 to t_4 was gradually decreasing, while the number density of the O_3 was the opposite. At the same time, the number density of the O_3 above the plate electrode can be approximated as uniformly distributed at the same instant except for the area below the needle tip. Figure 6 shows a graph of the average molar concentration of the O_3 over time in the entire discharge area, which indicates that the concentration of O_3 showed a cumulative upward trend as time passed.

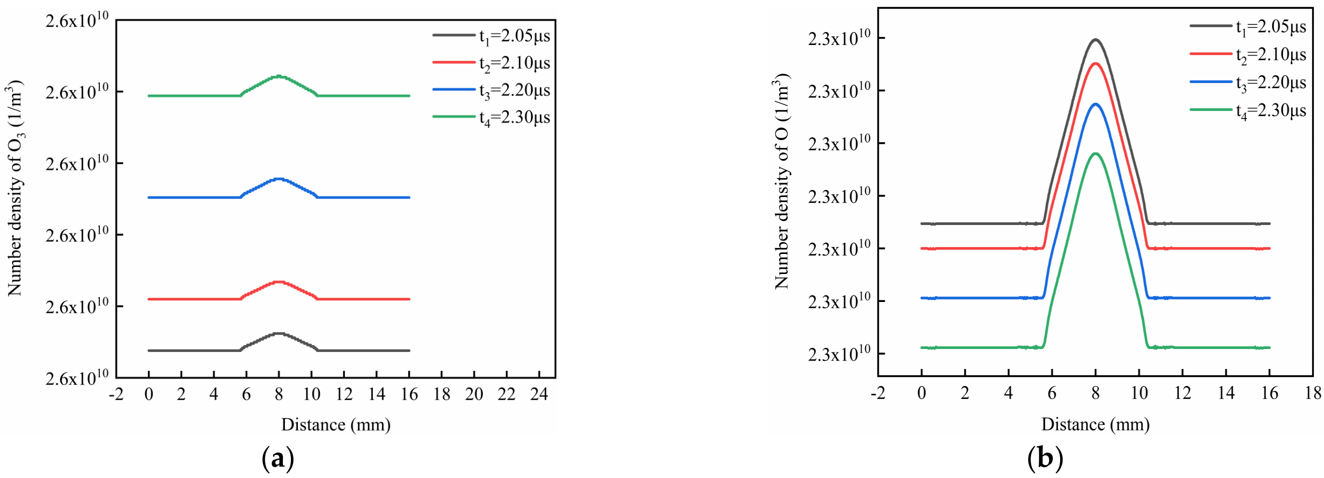

Figure 5. Horizontal density distribution of O and O_3 during the Trichel pulse: (**a**) Density of horizontal O_3; (**b**) Density of horizontal O.

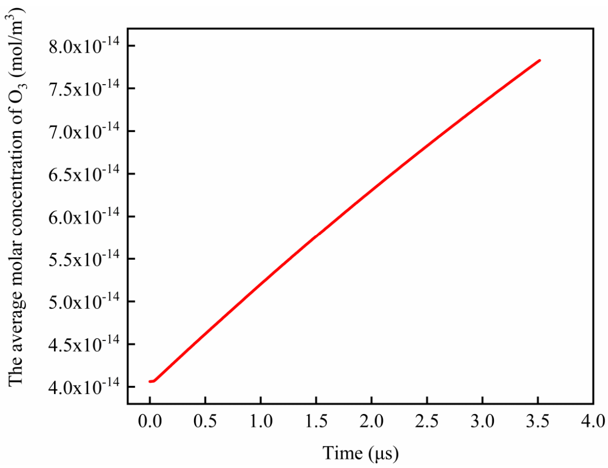

Figure 6. The average molar concentration of O_3 during the whole discharge process.

3.4.2. Generation Pattern of Hydrogen Peroxide (H_2O_2)

Exogenous active oxygen ROS (H_2O_2) can act as a signaling molecule to influence biological effects. In this paper, a simplified dry-air model was used; however, H_2O_2 is mainly generated by the combination of OH with OH, which is considered to be directly decomposed mainly by the electron bombardment of H_2O [36]. Therefore, considering the presence of water molecules in the actual air, this paper characterizes the H_2O_2 generation pattern in terms of the electron generation pattern.

As shown in Figure 4, the electron density of the cathode-sheath layer near the needle tip was nearly zero at the moments from t_1 to t_4, due to the repulsion of the cathode. The electron collapse started at the cathode of the needle tip and continued to diffuse and migrate to the anode plate, and consequently, H_2O_2 was also continuously produced. As shown in Figure 7, the dashed lines represent the local plots within this range. The variation pattern of the electron density was the same as that of the current pulse, and the electron density was maximum at the moment of the rising edge t_2, which gradually decreased with the development of the current pulse, but the electron density was greater than 0 throughout the period from t_1 to t_4. Thus, the concentration of H_2O_2 shows the same trend of cumulative increase with time and can be approximated as a uniform distribution of H_2O_2 above the plate electrode at the same instant except for the area below the needle tip.

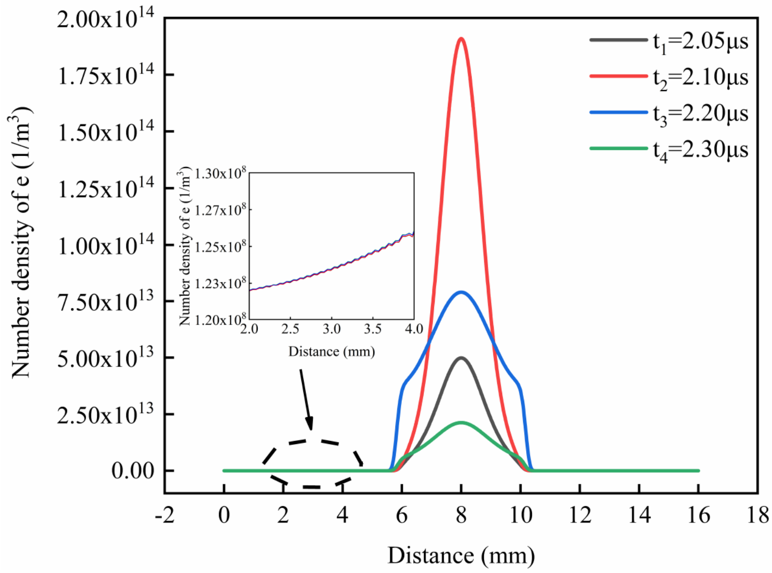

Figure 7. Horizontal distribution of electron density.

3.5. Generation Pattern of RNS

Exogenous active nitrogen RNS (NO) can break seed dormancy and promote germination and growth of biological seeds [24,28]. Figure 8 shows the graph of the average molar concentration of NO over time in the whole discharge area, which reveals that the concentration of NO tended to increase cumulatively with time. As shown in Table 2, NO was mainly produced by the reactions (O_3 + N => NO + O_2, O_2 + N => NO + O) and was approximately uniformly distributed horizontally at the same moment. The N played a primary part in the production of NO [37]. Under negative DC corona discharge, N was mainly supplied by the reaction (e + N_2^+ => 2N); meanwhile, it accumulated with time and was uniformly distributed above the plate electrode.

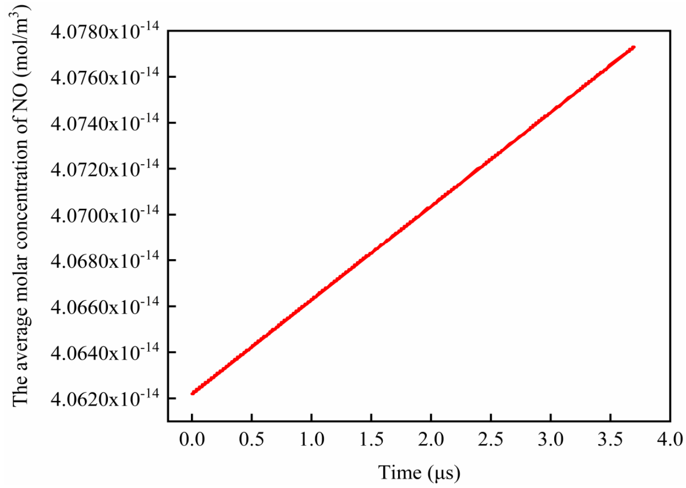

Figure 8. The average molar concentration of NO throughout the discharge process.

Table 2. Density of horizontal NO and N.

Time	NO ($1/m^3$)	N ($1/m^3$)
t_1	2.4514×10^{10}	2.4514×10^{10}
t_2	2.4515×10^{10}	2.4515×10^{10}
t_3	2.4517×10^{10}	2.4517×10^{10}
t_4	2.4520×10^{10}	2.4520×10^{10}

4. Conclusions

In this paper, a qualitatively validated air–chemical reaction system was used to simulate the DC negative corona discharge characteristics of needle-plate electrodes as well as the generation and distribution of active nitrogen oxides (RONS) capable of biologically promoting plant seeds.

The conclusions are as follows:

(1) During a Trichel pulse period, the rising and falling edges of the current correspond to the development of positive ions (N_2^+ and $O_2^{+)}$ in the cathode-sheath layer, respectively. Negative ions (O^- and O_2^-) move away from the cathode and diffuse continuously with the development of the electron collapse and the electric-field force, showing a typical layering phenomenon.

(2) Active oxygen ROS (O_3) is horizontally above the plate electrode except for the area below the needle tip, where its density is approximately uniformly distributed at the same instant, and the concentration of O_3 tends to increase cumulatively with time.

(3) The variation pattern of active oxygen ROS (H_2O_2) is the same as that of the current pulse, with the maximum density at the peak moment along the rise of the current pulse and a decrease with the development of the current pulse. The number density of H_2O_2 is greater than 0 throughout the pulse period. Thus, the concentration of H_2O_2 shows the same trend of cumulative increase with time and can be approximated as a uniform distribution of H_2O_2 above the grounding electrode plate at the same moment except for the area below the needle tip.

(4) The concentration of active nitrogen RNS (NO) increases cumulatively with time throughout the pulse period and is approximately uniformly distributed at the same moment in the levels.

Author Contributions: Conceptualization, J.S., F.J. and S.M.; methodology, J.S. and F.J.; software, J.S.; validation, X.L. (Xinhe Liu); formal analysis, J.S.; investigation, F.J.; data curation, X.L. (Xuejian Leng) and K.C.; writing—original draft preparation, J.S.; writing—review and editing, J.S. and F.J. All authors have read and agreed to the published version of the manuscript.

Funding: This work is supported by The Open Project of State Key Laboratory of Plateau Ecology and Agriculture, Qinghai University (No. 2019-ZZ-13).

Institutional Review Board Statement: Not applicable.

Informed Consent Statement: Not applicable.

Data Availability Statement: The data presented in this study are available upon reasonable request to the authors.

Acknowledgments: Thank you to the Foundation for its support and to each of the authors for their efforts.

Conflicts of Interest: The authors declare no conflict of interest.

References

1. Dordizadeh, P.; Adamiak, K.; Castle, G. Experimental study of the characteristics of Trichel pulses in the needle-plane negative corona discharge in atmospheric air. *J. Electrost.* **2016**, *88*, 49–54. [CrossRef]
2. Ma, Y.; Wang, X.; Ning, P.; Cheng, C.; Xu, K.; Wang, F.; Bian, Z.; Yan, S. Conversion of COS by corona plasma and the effect of simultaneous removal of COS and dust. *Chem. Eng. J.* **2016**, *290*, 328–334. [CrossRef]
3. Xu, X.; Zheng, C.; Yan, P.; Zhu, W.; Wang, Y.; Gao, X.; Luo, Z.; Ni, M.; Cen, K. Effect of electrode configuration on particle collection in a high-temperature electrostatic precipitator. *Sep. Purif. Technol.* **2016**, *166*, 157–163. [CrossRef]
4. Nie, S.; Qin, T.; Ji, H.; Nie, S.; Dai, Z. Synergistic effect of hydrodynamic cavitation and plasma oxidation for the degradation of Rhodamine B dye wastewater. *J. Water Process Eng.* **2022**, *49*, 103022. [CrossRef]
5. Uniyal, A.; Pal, A.; Srivastava, G.; Rana, M.; Taya, S.A.; Sharma, A.; Altahan, B.R.; Tomar, S.; Singh, Y.; Parajuli, D.; et al. Surface plasmon resonance biosensor sensitivity improvement employing of 2D materials and $BaTiO_3$ with bimetallic layers of silver. *J. Mater. Sci. Mater. Electron.* **2023**, *34*, 466. [CrossRef]
6. Xu, W.; Song, Z.; Luan, X.; Ding, C.; Cao, Z.; Ma, X. Biological Effects of High-Voltage Electric Field Treatment of Naked Oat Seeds. *Appl. Sci.* **2019**, *9*, 3829. [CrossRef]
7. Song, Z.; Ding, C.; Luan, X.; Chen, H. Review of research on biological effects of high-voltage corona electric field. *J. Nucl. Agric.* **2019**, *33*, 69–75. [CrossRef]
8. Luan, X.; Song, Z.; Du, J.; Wen, X.; Liu, H.; Yang, Z. Biological effects of high voltage corona electric field treatment of alfalfa. *Seed* **2019**, *38*, 18–23. [CrossRef]
9. Liu, M.; Tang, J.; Pan, C. Experimental study on the development process of DC positive and negative corona on needle plates in air. *High Volt. Technol.* **2016**, *42*, 1018–1027. [CrossRef]
10. Moreau, E.; Audier, P.; Benard, N. Ionic wind produced by positive and negative corona discharges in air. *J. Electrost.* **2018**, *93*, 85–96. [CrossRef]
11. Xu, L.P. Simulation Study on the Microscopic Discharge Mechanism of Air Needle-Plate Positive and Negative Corona. Master's Thesis, South China University of Technology, Guangzhou, China, 2020. [CrossRef]
12. Trichel, G.W. The Mechanism of the Negative Point to Plane Corona Near Onset. *Phys. Rev.* **1938**, *54*, 1078–1084. [CrossRef]
13. Feng, Q.; Huang, L.; Liu, D.; Wu, J.B.; Qi, H.W.; Dang, Z.M. Negative corona discharge characteristics of needle-plate and rod-plate electrode structures at different temperatures. *High Volt. Technol.* **2021**, *47*, 1847–1856. [CrossRef]
14. Liu, X. Research of the Mechanism and Characteristics in Air Discharge Based on the Fluid-Chemical Reaction Hybrid Model. Ph.D. Thesis, Chongqing University, Chongqing, China, 2012; pp. 41–64.
15. Liao, R.J.; Wu, F.F.; Yang, L.J.; Wang, K.; Zhou, Z.; Liu, K.L. Investigation on microcosmic characteristics of Trichel pulse in bar-plate DC negative corona discharge based on a novel simulation model. *Int. Rev. Electr. Eng.* **2013**, *8*, 504–513.
16. Liao, R.; Liu, K.; Wu, F.; Yang, L.; Zhou, Z. Simulation study on the characteristics of heavy particles during negative DC corona discharge at rod-plate electrodes. *High Volt. Technol.* **2014**, *40*, 7. [CrossRef]
17. Zhang, Y. DC Corona Discharge Characteristics and Its Spatial Ion Behavior. Ph.D. Thesis, Beijing University of Technology, Beijing, China, 2016.
18. Sera, B.; Spatenka, P.; Serý, M.; Vrchotova, N.; Hruskova, I. Influence of Plasma Treatment on Wheat and Oat Germination and Early Growth. *IEEE Trans. Plasma Sci.* **2010**, *38*, 2963–2968. [CrossRef]
19. Wang, M.; Chen, Q.; Chen, G.; Yang, S. Effects of atmospheric pressure plasma treatment on seed germination and growth and development of lettuce. *North China J. Agric.* **2007**, *6*, 108–113. [CrossRef]
20. Bailly, C. Active oxygen species and antioxidants in seed biology. *Seed Sci. Res.* **2004**, *14*, 93–107. [CrossRef]
21. Nishimura, H.; Hayamizu, T.; Yanagisawa, Y. Reduction of nitrogen oxide (NO_2) to nitrogen oxide (NO)by rush and other plants. *Environ. Sci. Technol.* **1986**, *20*, 413–416. [CrossRef]
22. Gong, B.; Yan, Y.; Zhang, L.; Cheng, F.; Liu, Z.; Shi, Q. Unravelling GSNOR-Mediated S-Nitrosylation and Multiple Developmental Programs in Tomato Plants. *Plant Cell Physiol.* **2019**, *60*, 2523–2537. [CrossRef]

23. Ali, Q.; Daud, M.; Haider, Z.M.; Ali, S.; Rizwan, M.; Aslam, N.; Noman, A.; Iqbal, N.; Shahzad, F.; Deeba, F.; et al. Seed priming by sodium nitroprusside improves salt tolerance in wheat (*Triticum aestivum* L.) by enhancing physiological and biochemical parameters. *Plant Physiol. Biochem.* **2017**, *119*, 50–58. [CrossRef]
24. Bethke, P.C.; Gubler, F.; Jacobsen, J.V.; Jones, R.L. Dormancy of Arabidopsis seeds and barley grains can be broken by nitric oxide. *Planta* **2004**, *219*, 847–855. [CrossRef] [PubMed]
25. Sarath, G.; Hou, G.; Baird, L.M.; Mitchell, R.B. ABA, ROS and NO are Key Players during Switchgrass Seed Germination. *Plant Signal Behav.* **2007**, *2*, 492–493. [CrossRef] [PubMed]
26. Bataller, M.; Veliz, E.; Riverol, Y.; Fernández, L.A.; Salomón, J.L.; Camilo, F.A.; Fernández, I. Effect of Ozone on Sprouting of Potato and Sugarcane Seeds: A Sustainable Alternative of Disinfection. *Ozone Sci. Eng.* **2021**, *43*, 451–460. [CrossRef]
27. Xu, W. Study on the Biological Effect of Seeds Treated with High Voltage Corona Electric Field. Master's Thesis, Inner Mongolia University of Technology, Hohhot, China, 2021. [CrossRef]
28. Huang, X. Study on the Effect of Pulsed Atmospheric Pressure Low Temperature Plasma on the Growth Characteristics of Ganoderma lucidum. Master's Thesis, Huazhong University of Science and Technology, Wuhan, China, 2021. [CrossRef]
29. Dobrin, D.; Magureanu, M.; Mandache, N.B.; Ionita, M.-D. The effect of non-thermal plasma treatment on wheat germination and early growth. *Innov. Food Sci. Emerg. Technol.* **2015**, *29*, 255–260. [CrossRef]
30. Cui, D.; Hu, X.; Yin, Y.; Zhu, Y.; Zhuang, J.; Wang, X.; Ma, R.; Jiao, Z. Quality enhancement and microbial reduction of mung bean (*Vigna radiata*) sprouts by non-thermal plasma pretreatment of seeds. *Plasma Sci. Technol.* **2022**, *24*, 045504. [CrossRef]
31. Liu, X.; He, W.; Yang, F.; Xiao, H.G.; Ma, J. Simulation and analysis of electron transport parameters in air discharge. *High Volt. Eng.* **2011**, *37*, 1614–1619.
32. Itikawa, Y.; Mason, N. Cross sections for electron collisions with water molecules. *J. Phys. Chem. Ref. Data* **2005**, *34*, 1–22. [CrossRef]
33. Tu, H.; Zhong, A.; Dai, D.; Li, L. Effect of electrode spacing on the generation of surface dielectric barrier discharge products. *J. Nanchang Univ. (Sci. Ed.)* **2022**, *46*, 266–276. [CrossRef]
34. Ning, W.; Dai, D.; Zhang, Y.; Han, Y.; Li, L. Effects of trace of nitrogen on the helium atmospheric pressure plasma jet interacting with a dielectric substrate. *J. Phys. D Appl. Phys.* **2018**, *51*, 125204. [CrossRef]
35. Fang, Z.; Lin, J.; Xie, X.; Qiu, Y.; Kuffel, E. Experimental study on the transition of the discharge modes in air dielectric barrier discharge. *J. Phys. D. Appl. Phys. A Europhys. J.* **2009**, *42*, 085203. [CrossRef]
36. Kuang, Y.; Zhang, C.; Hu, X.; Ren, C.; Chen, G.; Shao, T. Analysis of factors influencing nitrogen fixation by nanosecond pulsed liquid-phase discharge coupled with microbubbles. *J. Electrotechnol.* **2023**, *38*, 1–12. [CrossRef]
37. Pang, X.; Deng, Z.; Jia, P.; Liang, W. Numerical simulation of nitrogen oxide particle behavior in atmospheric plasma. *J. Phys.* **2011**, *60*, 345–353. [CrossRef]